Journal of Digital Imaging (2018) 31:520–533
https://doi.org/10.1007/s10278-018-0058-y

Detection of Lung Contour with Closed Principal Curve and Machine Learning

Tao Peng[1] · Yihuai Wang[1] · Thomas Canhao Xu[1] · Lianmin Shi[1] · Jianwu Jiang[1] · Shilang Zhu[1]

Published online: 15 February 2018

Abstract
Radiation therapy plays an essential role in the treatment of cancer. In radiation therapy, the ideal radiation doses are delivered to the observed tumor while not affecting neighboring normal tissues. In three-dimensional computed tomography (3D-CT) scans, the contours of tumors and organs-at-risk (OARs) are often manually delineated by radiologists. The task is complicated and time-consuming, and the manually delineated results will be variable from different radiologists. We propose a semi-supervised contour detection algorithm, which firstly uses a few points of region of interest (ROI) as an approximate initialization. Then the data sequences are achieved by the closed polygonal line (CPL) algorithm, where the data sequences consist of the ordered projection indexes and the corresponding initial points. Finally, the smooth lung contour can be obtained, when the data sequences are trained by the backpropagation neural network model (BNNM). We use the private clinical dataset and the public Lung Image Database Consortium and Image Database Resource Initiative (LIDC-IDRI) dataset to measure the accuracy of the presented method, respectively. To the private dataset, experimental results on the initial points which are as low as 15% of the manually delineated points show that the Dice coefficient reaches up to 0.95 and the global error is as low as 1.47×10^{-2}. The performance of the proposed algorithm is also better than the cubic spline interpolation (CSI) algorithm. While on the public LIDC-IDRI dataset, our method achieves superior segmentation performance with average Dice of 0.83.

Keywords Lung contour · Principal curve · Closed polygonal line algorithm · Machine learning

Introduction

With the advancement of medical imaging technology, the amount of data obtained in the clinical images has increased exponentially. The important information for organ diseases can be quantitatively provided by the clinical images, while quantification is often manually implemented in some clinics. In order to speed up the manual task and reduce workload, combining computer-aided diagnosis (CAD) with automatic detection method is becoming a research hotspot. A contour is an ordered set of data points with segments connecting them into a piecewise-defined curve. The obtained contour can be represented in a simple form, and it can be useful in solving various problems such as shape matching and retrieval, character recognition, and medical image analysis [1]. In order to overcome the interference factors, such as noise, occlusion, and artifacts, both detection and representation problems will face a big challenge. Therefore, accurate detection of region of interest (ROI) contour of medical image is necessary.

Most current medical image edge detection techniques can be categorized as feature-classify approaches [2–5], threshold segmentation approaches [6, 7], and contour curve detection approaches [8–11]. Tang et al. [12] have developed a splat feature classification method to detect retinal hemorrhage. The authors show that an area under the receiver operating characteristic (ROC) curve [13] is 0.96 and 0.87 at the splat and the image level, respectively. Maggio et al. [14] have successfully exploited hybrid feature selection algorithm to prune unimportant features and realize rapid computation. However, both of their techniques only test a single dataset. In Ref. [15], Pu et al. have presented a computerized scheme to automatically segment the 3-D human airway tree based on selecting a multithreshold. However, the author does not use the Dice coefficient [16, 17] treated as a standard for assessing similarity to prove the performance of the proposed method.

✉ Tao Peng
sdpengtao401@gmail.com

✉ Yihuai Wang
yihuaiw@suda.edu.cn

[1] School of Computer Science & Technology, Soochow University, No.1 Shizi Road, Suzhou, Jiangsu 215006, China

The contour curve detection approach has an impact on describing the shape of the specific organ, where the contour curve consists of the data points of the edge [18]. Comparing with the other two approaches, the form of experimental results obtained by the contour curve detection approach can save more storage space, while the shape feature of the specific organ can be easily extracted.

The main purpose of contour detection is to use shape representation models to approximately represent a boundary curve [18, 19]. Related work can be found on studies about shape representation [20–22] and curve approximation [23, 24]. Shepherd et al. [25] have proposed a segmentation method combined statistical shape model (SSM) with online and offline learning method based on shape priors, while Song et al. [26] have devised a method for multi-object segmentation using context and shape prior in a 3-D graph-theoretic framework with good accuracy. However, both of them only use a subset of the whole shape as the prior shape, where it will ignore some information. Zhang et al. [27] have exploited dictionary learning and local shape prior model to detect the ROI in whole body CT with increased overall accuracy. However, the author did not consider noisy inputs. Heibel et al. [28] have combined Markov random fields with B-spline curve algorithm to approximate a contour curve that the sequence of points was previously known. Aquino et al. [29] have used edge detection and morphological methods followed by the Circular Hough Transform to achieve the optic disc boundary curve approximation. In Ref. [29], they do not compare their result to the ground truth.

Among many other contour detection methods, principal curve technique is a useful tool for noisy inputs and can obtain a robust result [30]. Principal curve was described by Hastie [31] as a smooth curve which passes through the "middle" of a set of data points. The notion is successfully utilized in many applications such as skeletonization [32, 33] and curvilinear feature detection from data points [34]. In Ref. [30], the authors have used principal curve to extract the coronary artery centerlines. Further, the artificial neural network [2–4], which is treated as a classifier, can be well used to detect the tumor regions from non-tumor regions. Thus, principal curve combining with machine learning is a promising candidate in detecting discriminative information from the dataset [35, 36].

Lavdas et al. [37] have used classification forest (CF), Convolutional Neural Networks (CNN) and a multi-atlas (MA) approach for multi-organ segmentation, respectively. The CNN algorithm can have the capability of learning complex data associations, while the training configuration is too complex. In Ref. [38], Tseng et al. have proposed a deep reinforcement learning (DRL) method for dynamic clinical decision making in adaptive radiotherapy. However, development of the method into a fully credible autonomous system would require further validation on larger multi-institutional datasets. Ma et al. [39] have utilized Cascade convolutional neural networks to evaluate a fully automatic detection of thyroid nodules from 2D ultrasound images, while Shaukat et al. [40] have developed a fully automatic detected method to lung nodules using a hybrid feature set with Support Vector Machine (SVM) classifier. However, both of them cannot detect micronodules (< 3 mm) accurately. Considering that deep learning is more suitable for the large dataset [41, 42], we choose backpropagation neural network for training.

In this work, we use less than 15% points of ROI as an approximate initialization; the approximate contour of lung image can be obtained by combining closed polygonal line and backpropagation neural network model (CPL-BNNM) algorithm. Experimental results show that the obtained lung contours can be smoothly and accurately expressed, when the relation between the data points and their corresponding projection indexes is identified by training with BNNM. The computational complexity and the workload of radiologists can be well reduced. At the same time, comparing with the cubic spline interpolation (CSI) algorithm, the performance of the proposed algorithm can be further proved.

Materials and Methods

This section firstly introduces brief discussions on two theories that are relevant to this article, which is named principal curve and machining learning, respectively. Then the overall process of the proposed algorithm will be described. Finally, the quantitative evaluation parameters which consist of global error and Dice coefficient can be proposed.

Principal Curve

K-Segment Principal Curve

In d-dimensional space R^d, when the curve $f(t)$ satisfies the three conditions, firstly $f(t)$ does not intersect itself, secondly $f(t)$ has finite length inside any bounded subset in d-dimensional space R^d, and thirdly $f(t)$ is self-consistent, then $f(t)$ is regarded as a principal curve. The property of the principal curve $f(t)$ can be defined that $f(t) = E(X| t_f(X) = t)$. Figure 1 shows the projection from the points to the curve, The projection index $t_f(x_i)$ is a value of t which makes $f(t)$ closest to x_i.

$$t_f(x_i) = \sup\{t : \|x_i - f(t)\| = \inf_\tau \|x_i - f(\tau)\|\} \quad (1)$$

The goodness of the method can be confirmed by constraining the length of the curve. For data distribution X, we say that f is described as k-segment principal curve (KSPC) where the constrained length of principal curve is L. On all curves which lengths are not larger than L, the

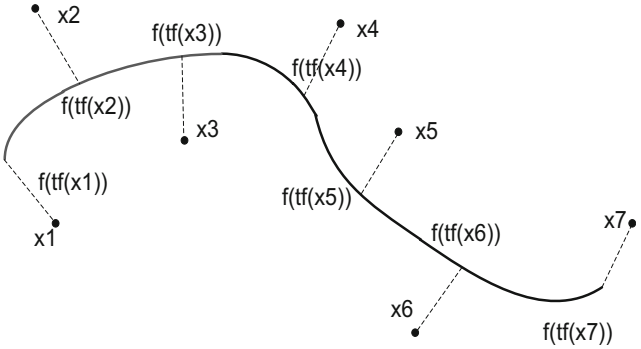

Fig. 1 Projection from the points to the curve

minimized distance function of f is designed using the following equation:

$$\Delta(f) = \Delta(X, f) = E[\Delta(X, f)] = E\left[\left\|X - f\left(t_f(X)\right)\right\|^2\right] \quad (2)$$

Kegl et al. [33] give the convergence confirmation of the KSPC; it can guarantee the learning ability of the principal curve and propose the polygonal line algorithm for finding the KSPC.

Polygonal Line Algorithm

The two crucial steps of the Polygonal Line (PL) algorithm are the projection and vertex optimization step.

(1) In the projection step, the data points are classified according to which segment or vertex they project. Let f be a polygon curve composed of vertexs $v_1, v_2, \ldots, v_{k+1}$ and line segments $s_1, s_2, \ldots, s_k$,. s_i connects v_i, v_{i+1}, where in $i \in (1, k)$, i is a positive integer. The dataset X_n is divided into 2k + 1 disjoint sets which consist of $(V_1, V_2, .., V_{k+1})$ and $(S_1, S_2, .., S_k)$, and they are called the sample points which belong to the vertex V_i or line segment S_i.

$$V_i = \{x \in X_n : \Delta(x, v_i) = \Delta(x, f), \Delta(x, v_i) < \Delta(x, v_m), m = 1, 2, .., i-1\} \quad (3)$$

$$S_i = \{x \in X_n : x \notin V, \Delta(x, s_i) = \Delta(x, f), \Delta(x, s_i) < \Delta(x, s_m), m = 1, 2, .., i-1\} \quad (4)$$

(2) In the vertex optimization step, the position of each vertex is adapted on the principle that distance from the sample points to the principal curve is the smallest. The gradient-based minimization method which minimizes the penalty distance function makes the position of the point changed while changing each line segment.

$$G_n'(f) = \Delta_n'(f) + \lambda_p p(f) \quad (5)$$

Where $G_n'(f)$ produced by line segment s_i infinitely extense to line segment s_i' on f is the minimized penalty distance function. When $\Delta_n'(f)$ shows the fitting level is small, the fold line will be close to the fitting data. $p(f)$ is the average curvature penalty, which affects the smooth degree of the fold line. λ_p balance between $\Delta_n'(f)$ and $p(f)$ is the penalty factor, where $\lambda_p = \lambda_p' k n^{-1/3} \Delta_n \left(f_{k,n}\right)^{1/2} r^{-1}$, the value of λ_p is optimally set to a constant 0.13 by experiment vertification [43].

In the vertex optimization step, the length constraint can be transformed into the angle constraint; the smooth principal curve can be obtained by penalizing angle. The constraint condition $P(v_i)$ of the vertex v_i can be obtained by

$$P(v_i) = \begin{cases} 2\mu_+(v_i) + \pi(v_{i+1}) \text{ if } i = 1 \\ \mu_-(v_i) + \pi(v_i) + \pi(v_{i+1}) \text{ if } i = 2 \\ \pi(v_{i-1}) + \pi(v_i) + \pi(v_{i+1}) \text{ if } 2 \le i \le k-1 \\ \pi(v_{i-1}) + \pi(v_i) + \mu_+(v_i) \text{ if } i = k \\ \pi(v_{i-1}) + 2\mu_-(v_i) \text{ if } i = k+1 \end{cases} \quad (6)$$

Where γ_i is the angle which vertex is v_i and r is the radius of the data described.

Machine Learning

BNNM is the machine learning algorithm for training a multilayer neural network. It trains multilayer feedforward neural networks which contains iterative gradient descent property. In this section, we summarize the essential equations which are used to implement the BNNM.

For a set of training vectors X, it exists output vector set Y which is associated with X. The mean square error between the actual output of the neural network and the expected output can be written as

$$E_k = \frac{1}{N} \sum_{t=1}^{N} (y_{\mathrm{kt}} - c_{\mathrm{kt}})^2 \quad (7)$$

where y_{kt} is the actual output and c_{kt} is prediction output.

The goal of the algorithm is to minimize the global error function E according to the following equation:

$$E = \sum_{k=1}^{m} E_k \quad (8)$$

where m is the cardinality of E. The training process terminates with positive results when the global error function E reaches the presetted minimum value. Otherwise, the training process will keep on running. The training process successes when E reached the presetted minimum value. On the other hand, the training process fails when E does not reach the presetted minimum value within the given epoch number.

Proposed Algorithm

When we deal with the dataset, the first principal component line is regarded as the starting step. The projection indexes of

dataset could not be correctly described when we calculate the data sequences with the PL algorithm; the expected result could not be obtained on training step. Aiming at the characteristics of this problem, the CPL-BNNM algorithm is proposed to find the principal curve algorithm. The flowchart of the proposed CPL-BNNM algorithm is exhibited in Fig. 2.

Obtain Data Sequences

In the first step, normalize the dataset $\{x_1, x_2, .., x_n\}$ and record the coordinates $(x_i, y_i)(i = 1, 2, .., n)$ of the dataset. Then in order to introduce uniformly, the dataset which consists of the coordinate form is used to handle. Normalize all the dataset to the range $\{(-1, -1)\sim(1, 1)\}$.

In the second step start with a small square as the starting step, where small squares are

$$V = \{V_1, V_2, V_3, V_4, V_5\} = \{(-0.1, -0.1), (-0.1, 0.1), (0.1, 0.1), (0.1, -0.1), (-0.1, -0.1)\}$$

In the third step, enter into the outer loop and calculate the value of the outer loop distance function.

In the fourth step, run the inner loop and adjust the position of each vertex. When the angle between lines is greater than 90^o and the shape is closed, by projecting the dataset to the line and the vertex projection, the distance function from data points to the curve can be calculated. During the value of distance function becomes smaller, the position of vertex will be changed under the principle of the vertex optimization step. Comparing the value of the current distance function with the value of the last inner loop distance function, when the reduced value is smaller than the max distance deviation $\Delta s = 0.002$, it reaches the inner loop stop condition and executes the fifth step. Otherwise, the new vertex will be added and the fourth step will be re-executed.

In the fifth step, comparing the value of the current distance function with the value of the previous outer loop distance function, when the reduced value is smaller than the max distance deviation $\Delta s = 0.002$, the outer loop stop condition is reached, and a closed polygon formed by a piecewise straight line can be obtained, then it goes to the sixth step. Differently, the new vertex will be added, and it goes to the third step to re-execute the outer loop operation step.

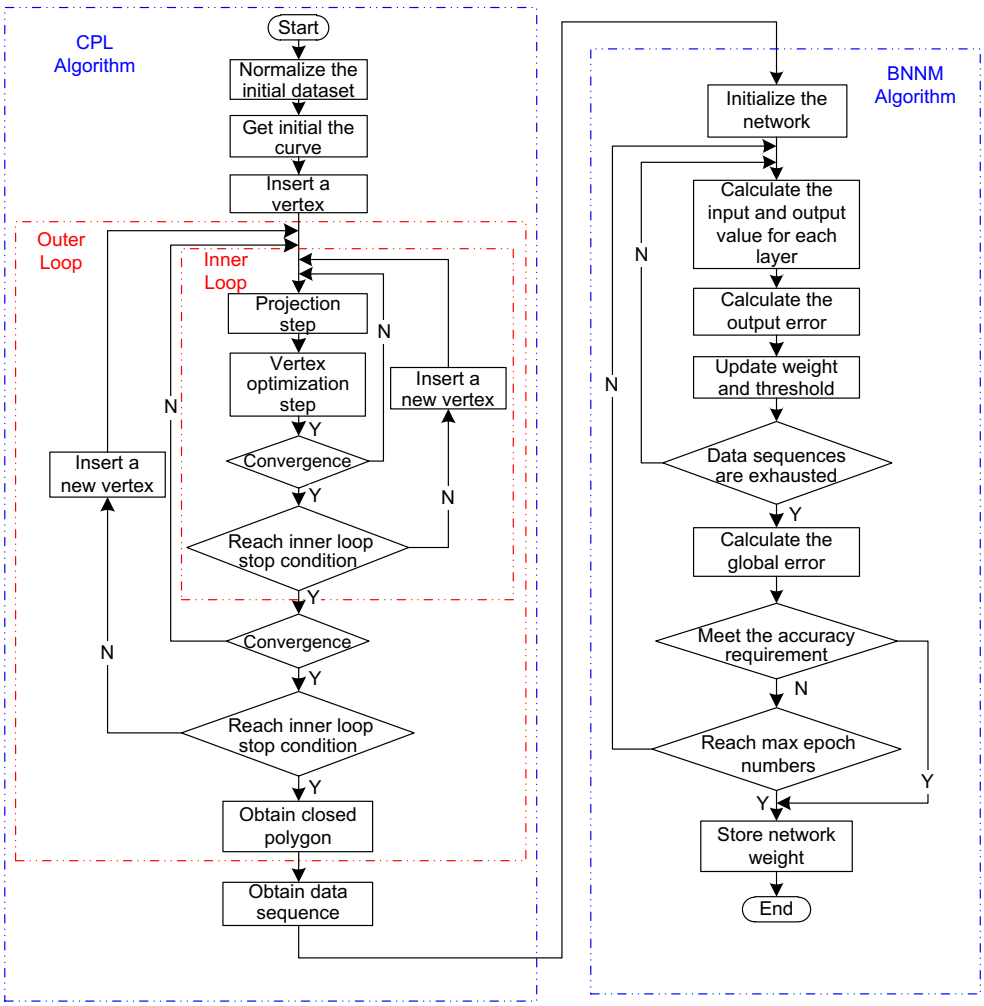

Fig. 2 The flowchart of the proposed CPL-BNNM algorithm

In the sixth step, the projection indexes $\{t_1, t_2, \ldots, t_n\}$ of the dataset can be achieved by projecting the dataset to the closed polygon. According to the sequence of projection index t_i defined from small to large, the dataset $(x_i, y_i)(i = 1, 2, .., n)$ is sorted. Finally, the data sequences consist of the ordered projection indexes, and the corresponding data points $\{(t_i, (x_i, y_i)), i = 1, 2, \ldots, n, 0 \le t_1 < t_2 < \ldots < t_n \le 1\}$ can be obtained.

Training

By looking for a continuous, differentiable, and integrable smooth function, the principal curve is used to approximate the distribution of the dataset points. Due to the complicated relationship of function, simple regression method cannot be well fitted. The BNNM minimizes the global error of dataset to approximate function and fit curve to obtain a smooth principal curve.

BNNM which consists of three layers (an input layer, a hidden layer, and an output layer) is a multi-layer perception machine. In order to make the hidden layer suitable for all useful functions, the multilayer network must have a nonlinear activation function which is used for multiple layers. The paper chooses sigmoid function is specified that

$$f(x) = \frac{1}{1 + e^{-\lambda x}} \tag{9}$$

The steepness parameter λ determines the active region of the activation function. When the steepness parameter λ is from infinity to zero, the sigmoid function alters from the unit step function to the constant value of 0.5 as well.

The feedforward network contains the hidden layer which can approximate any continuous function. Considering that the feedforward network contains one hidden layer is a general function approximator, this paper selects the BNNM with one hidden layer to train. In order to find the relation between the ordered projection indexes and the corresponding data points, the x and y can be regarded as the continuous function $x(t)$ and $y(t)$ on t respectively, where the projection index is taken as the independent variable, and the coordinates of the initial data points are the dependent variable. The corresponding mathematical expression of the principal curve which is expressed as

$$f(t) = ((x(t)), (y(t))) \tag{10}$$

$$= \left(\frac{1}{1 + e^{-\left(\sum_{i=1}^{N} \frac{1}{1+e^{-(\mathrm{tw}_i - T_i)}} v_{i,1} - r_1 \right)}}, \frac{1}{1 + e^{-\left(\sum_{i=1}^{N} \frac{1}{1+e^{-(\mathrm{tw}_i - T_i)}} v_{i,2} - r_2 \right)}} \right)$$

The corresponding parameters are denoted as follows:

N the number of the neurons at the hidden layer
w_i the weight from the input layer to the i-th neuron at the hidden layer
T_i the output threshold of the i-th neuron at the hidden layer
$v_{i,k}$ the weight from the i-th neuron at hidden layer to the k-th neuron at the output layer
r_k the output threshold of the k-th neuron at the output layer

$$i = 1, 2, .., N; k = 1, 2.$$

Quantitative Evaluation

In order to confirm the performance of the proposed CPL-BNNM algorithm, the Dice coefficient and the global error will be used.

Global Error

In the BNNM, we train the BNNM to achieve the goal by minimizing the global error E, where the global error E is the sum of the mean square E_k and the mean square error E_k which represents the deviation between the actual output and the expected output in the neural network.

Dice Coefficient

To evaluate the accuracy of the proposed CPL-BNNM algorithm, the Dice coefficient is used to quantify the overlap between the detection results and the manually drawn contours by radiologists. The Dice coefficient treated as a standard for assessing similarity is calculated with

$$d = 2\frac{|A \cap B|}{|A| + |B|} \tag{11}$$

where the A and B denote the coordinates of points which belong to the edge of the detection result; the A is the detection result of the proposed algorithm; the B is the detection result by radiologists manually.

Results and Discussions

In this section, in order to prove the performance of the proposed CPL-BNNM algorithm, we use the private high-resolution lung dataset and the public Lung Image Database Consortium and Image Database Resource Initiative (LIDC-IDRI) dataset for contour detection, respectively. The private dataset is acquired by 3D-CT scans in which the detection results are compared with the manually delineated contours by overlapping ratio. All contours of ROIs are manually delineated by professional radiologists as a reference for

evaluation. The detection results of the proposed algorithm can be evaluated quantitatively and qualitatively. The anonymous 3D-CT dataset is provided by the Second Affiliated Hospital of Soochow University. The dataset format is DICOM; the image size is 512×512, while the public LIDC-IDRI dataset of CT scans was acquired from the Lung Imaging Database Consortium (LIDC) and Image Database Resource Initiative (IDRI) [44]. The experiments run on a computer with 2CPU i5-4590 3.3GHz, 2GB RAM.

The over-oscillation of the system is resulted by high momentum parameter. On the other hand, local minimization will be caused by low momentum parameters in which the system training will slow down. Hence, the momentum parameter α will be set 1 in the BNNM. In the CPL algorithm, the range of the distance deviation is $\Delta s \in [0,0.002]$ and the curvature penalty factor is $\lambda_p^{'} = 0.13$. The following experimental part will give a comparison of the actual dataset; the blue lines show the contours obtained by the proposed algorithm, and yellow lines show the manually delineated contours.

Contour Detection under Different Learning Rates on Private Dataset

In order to obtain the corresponding training time, the Dice coefficient and E at different learning rates, the number of neurons at the hidden layer is set to 10 and the number of epochs is set to 5×10^5. Figure 3 shows the corresponding training times which obtained at different learning rates from 0.2 to 0.7. As can be seen from Fig. 3, due to the smaller number of points in *Lung A*, the overall training time is shorter than *Lung B* and *Lung C*. In the whole view, with the increasing learning rate, the training time is always increasing until the learning rate reaches 0.5. After that, the training time almost remains the same. In *Lung B* and *Lung C*, with the appropriately initialized learning rate, when the learning rate is varied from 0.4 to 0.5, the training time increases slightly, where the BNNM converges very fast.

Figures 4 and 5 show the Dice coefficient and E at different learning rates. The Dice coefficient represents the overlap between the detection contours obtained by the proposed algorithm and the manually drawn contours by radiologists, where E represents the global error of the proposed algorithm. From the whole view of Figs. 4 and 5, the trends of the Dice coefficient and E are almost opposite at the same learning rate. To *Lung A* in Fig. 4, the BNNM can obtain the optimal Dice coefficient very fast with the different learning rates. When the learning rate is 0.4, the max Dice coefficient is as high as 0.95 in which the initial points are only a small number of points. In *Lung B*, the iterative process is unstable, which is caused by rapidly altering learning rate; the curve of the Dice coefficient suddenly drops when the learning rate is 0.3. From Fig. 5 in *Lung A*, we can see that when the curve of the E is at the concave vertice, the corresponding optimally learning rate η is 0.4 and the E is reduced to 1.47×10^{-2}. After that, the algorithm converges and the E is close to constant. Figure 6 shows the comparison between the contours obtained by the proposed CPL-BNNM algorithm and the manually delineated contours at different learning rates.

In the BNNM, the selection of learning rate is critical. More steps are needed to achieve acceptable results with small learning rates. On the contrary, when the learning rate is too large, it will lead to oscillation near extreme points which prevents to converge. In order to prove the influence of epochs number and the number of neurons in the BNNM, a compromise scheme is selected to set the learning rate $\eta = 0.5$.

Contour Detection under Different Numbers of Neurons at the Hidden Layer on Private Dataset

At the hidden layer, the selection of neuron number has a great impact on the learning accuracy and training speed. Figures 7 and 8 show the results of the Dice coefficient and E with different numbers of neurons, respectively. As illustrated in

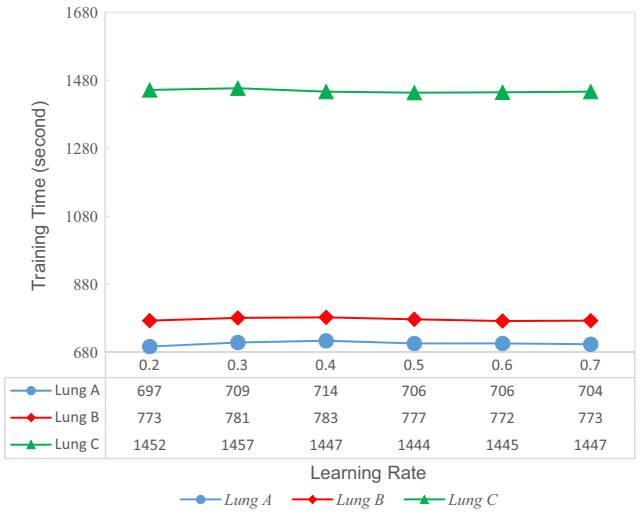

Fig. 3 Corresponding training times at different learning rates

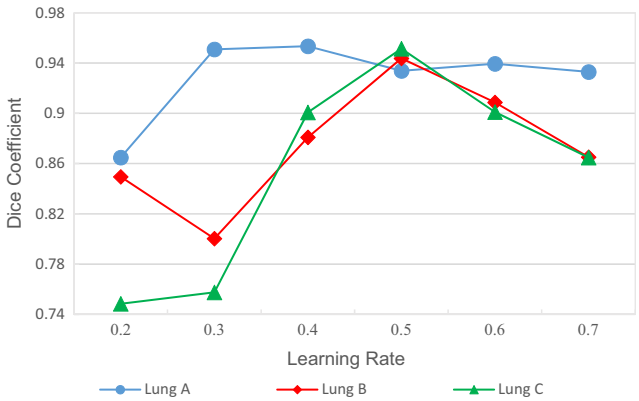

Fig. 4 Corresponding Dice coefficient at different learning rates

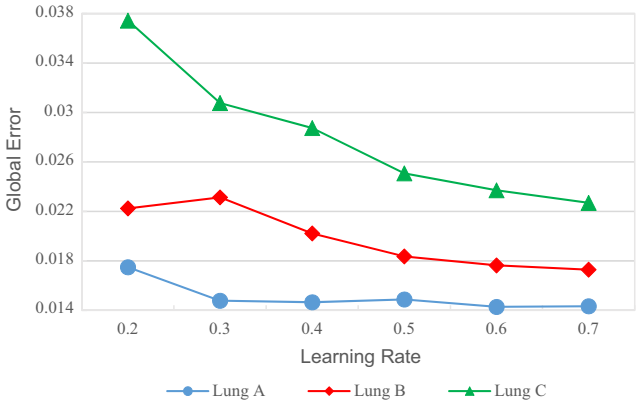

Fig. 5 Corresponding E at different learning rates

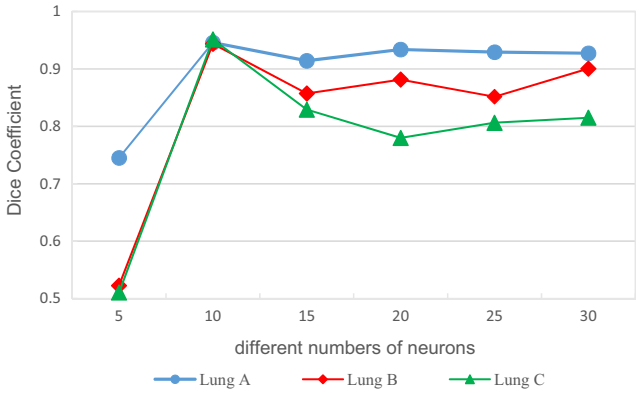

Fig. 7 Corresponding Dice coefficient at different numbers of neurons

Fig. 7 and 8, when the neuron number is 5, the Dice coefficient is as low as 0.51, while the E reaches up to 6.08×10^{-2}. A complex problem fails to be dealt with the BNNM, in case the number of neurons is not enough at the hidden layer. From Fig. 7, with increasing number of neurons at the hidden layer, training time sharply increases. Meanwhile, it may lead to overtraining and reduce the ability of anti-interference; the Dice coefficient has a greater fluctuation. Because of more points in *Lung B* and *Lung C*, the max fluctuation of the Dice coefficient is 44.08%. Figure 9 shows the comparison between the detected contours and the manually drawn contours with different numbers of neurons at the hidden layer. The promising results prove the feasibility of the algorithm.

Contour Detection under Different Numbers of Epochs on Private Dataset

In this part, we use the three-layer feedforward neural network which consists of ten neurons at the hidden layer. As can be seen from *Lung A* and *Lung C* in Fig. 10, the Dice coefficient increases with more complex BNNM when the number of epochs increases; it leads the BNNM to be more complex.

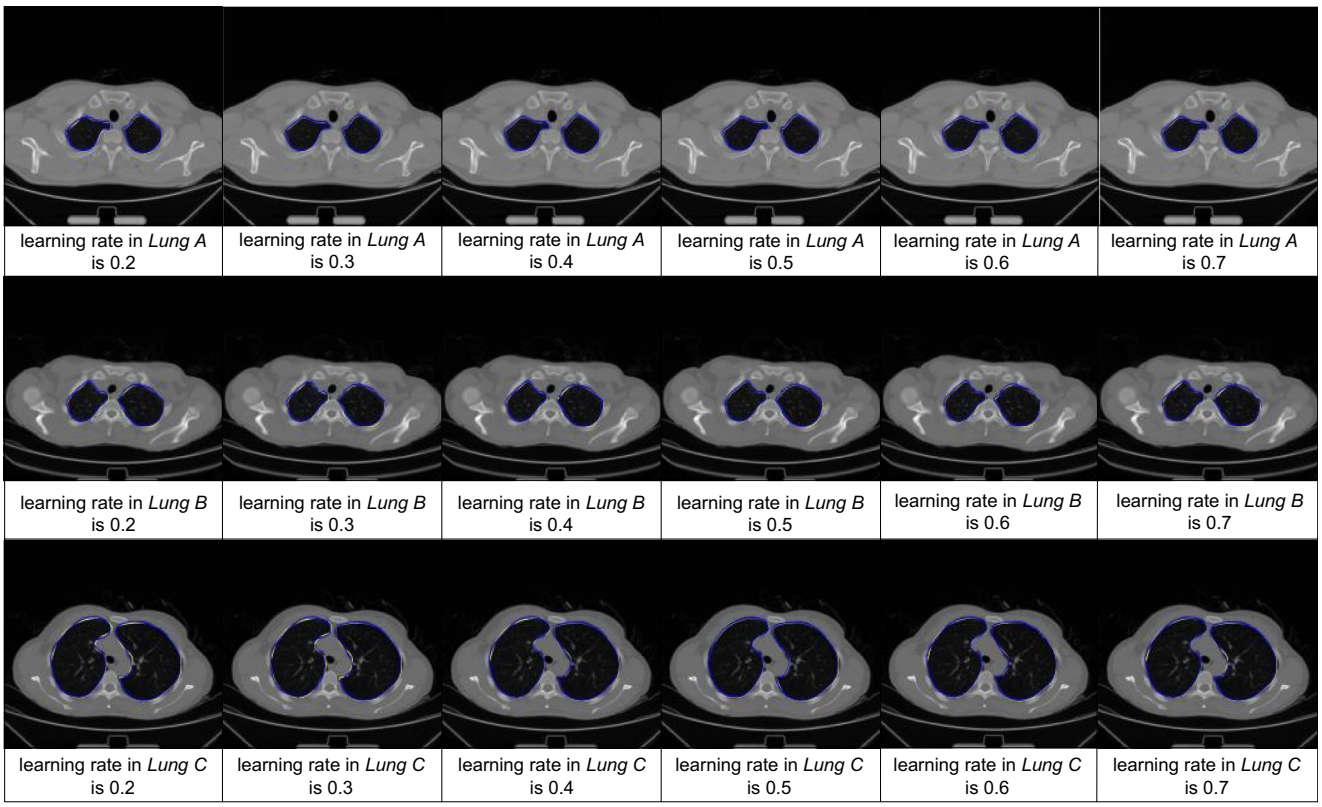

Fig. 6 Comparison between the contours obtained by the proposed CPL-BNNM algorithm and the manually delineated contours at different learning rates

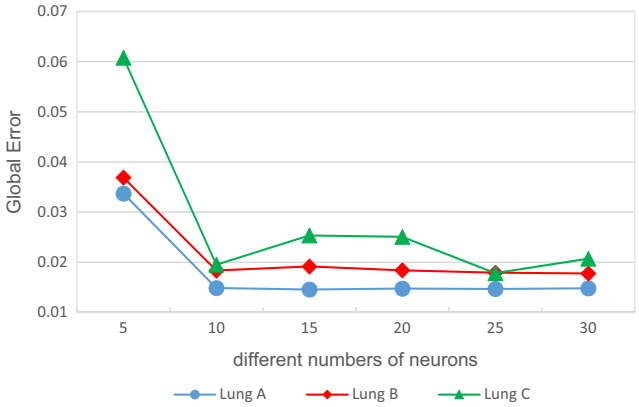

Fig. 8 Corresponding E at different numbers of neurons

The dice reaches its peak when the number of epoches reaches 5×10^5, where the Dice of *Lung A* is 0.94 and the Dice coefficient of the *Lung C* is 0.95. At this time, the BNNM goes on to train, the Dice coefficient does not rise but drop. One possible reason is that at this time, the complexity of the BNNM reaches a certain extent in which overfitting can be a result with excessively increased number of epochs. The common way to avoid the overfitting phenomenon is to require the standard regularization methods, early stopping, or dropout [45, 46], considering that overfitting is not a big problem with our method and therefore we do not pay more attention to deal with it. Moreover, according to the variation of E shown in Fig. 11, when the epoch training time passes, the E decreased constantly with longer training time; however, the result tend to be more stable with epochs greater than 5×10^5.

Figure 12 shows the comparison between the contours obtained by the proposed algorithm and the manual contours at different numbers of epochs. Comparing the dataset in Fig. 12, it can be found that the overall overlapping ratio of *Lung A* is higher than the second and the third. With the increasing number of epochs, the overlaps of the dataset are increasing as well. When the epochs number of *Lung A* reaches 3×10^5, the curve of overlapping ratio attains steady state. However, because of more points in *Lung B* and *Lung C*, the curve of overlapping ratio is nearly stable until the epochs number reaches 4×10^5. The overlapping ratio curves of the actual dataset are in good agreement with the trend of the Dice coefficient and E. Totally, the contour of the principal curve obtained by the proposed CPL-BNNM algorithm can truthfully summarize the manually delineated contours.

Contour Detection under Different Algorithms on Private Dataset

To prove the effectiveness of the proposed algorithm in lung contour detection, we choose the fitting accuracy to be criteria for judging. The existing principal algorithms are chosen to compare with the proposed CPL-BNNM algorithm. Nowadays, the

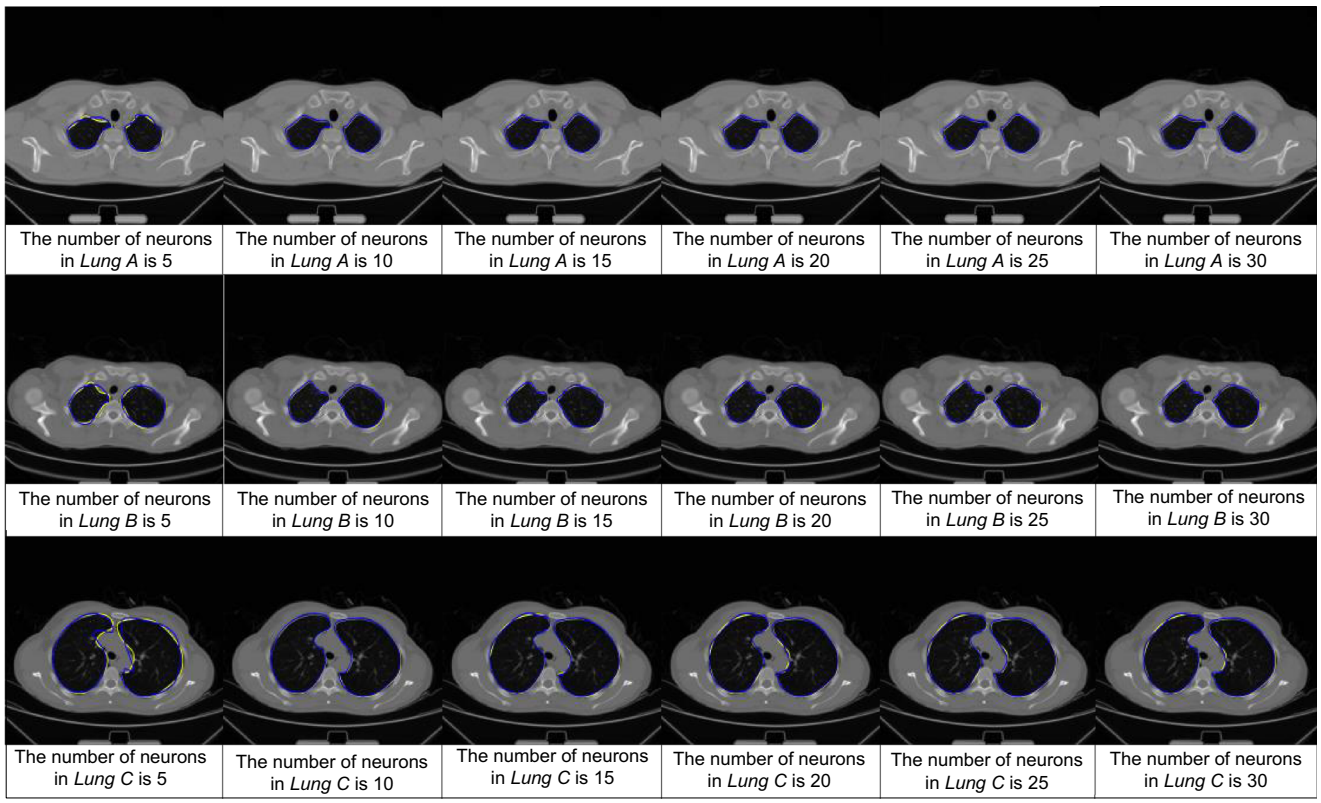

Fig. 9 Comparison between the detected contours and the manual drawn contours with different numbers of neurons at the hidden layer

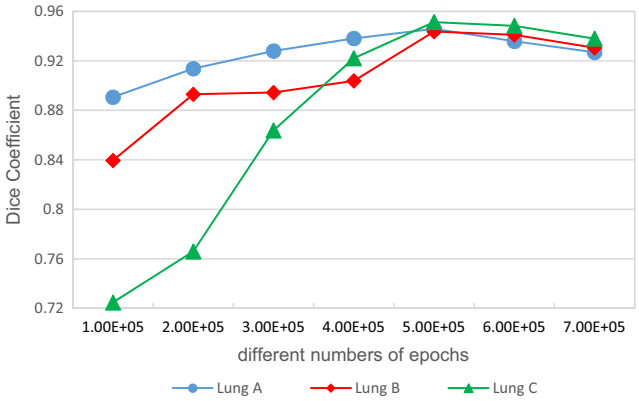

Fig. 10 Corresponding Dice coefficient at different numbers of epochs

current main algorithms are the least squares (LS) algorithm and the cubic spline interpolation (CSI) algorithm. The LS algorithm is recommended to use by the International Electrotechnical Commission. And the CSI algorithm which has a high accuracy can be modeled for the closed curve.

To the closed dataset, the LS algorithm needs to segment processing. Hence, the results obtained by the LS algorithm will be affected. In summary, the CSI algorithm is chosen to compare with the proposed CPL-BNNM algorithm; both algorithms only use as low as 15% of the manual points to be initial points. The parameters of the proposed CPL-BNNM algorithm are selected as follows: the learning rate is 0.5, the number of neurons is 10, and the number of epochs is 5×10^5. Figure 13 shows the global comparison graph of curve fitting. Figure 14 shows the partial magnification graph of curve fitting. In order to make the results more intuitive, the red solid circles are used to describe the approximate trajectory of the initial points. When the red solid circles are loaded into the curve of the proposed CPL-BNNM and CSI algorithm respectively, it is easy for analysis.

Figure 13(A), (B) show the left lung image dealt by the CSI and CPL-BNNM algorithm, respectively. Figure 13(C), (D) show the right lung image dealt by the CSI and CPL-BNNM algorithm, respectively. The $\triangle(f)$ represents the global European square distance function regarded as the evaluation index. In principle, when the $\triangle(f)$ decreases, the curve f is much closer to the dataset, while the similarity of the proposed results is much higher. Thus, the phenomenon in the dataset is similar, *Lung A* will be used as an example to analyze. In *Lung A*, compared with the $\triangle(f)$ of the left lung image in Fig. 13(1A), (1B), the $\triangle(f) = 1.44 \times 10^{-2}$ obtained by the CSI algorithm is much larger than the $\triangle(f) = 2.83 \times 10^{-3}$ achieved by the proposed CPL-BNNM algorithm. Meanwhile, to the right lung image in Fig. 13(1C), (1D), the $\triangle(f) = 1.78 \times 10^{-2}$ received by the CSI algorithm is much larger than the $\triangle(f) = 4.36 \times 10^{-3}$ obtained by the proposed CPL-BNNM algorithm. Through the nine compared results, it can be concluded that when the discrete data points are excessively many, the inverse matrix becomes more complicated, while the fitting result of CSI algorithm is not good. The proposed CPL-BNNM algorithm contains feedforward neural network with the hidden layer which can approximate any continuous function with arbitrary precision. It can be seen that the fitting precision of the proposed CPL-BNNM algorithm is better than that of the CSI algorithm.

Furthermore, although the closed curve can also be fitted by the CSI algorithm, the sequence of the projection indexes needs to be obtained manually during collecting dataset, where the complexity of operation is increased. In this paper, the projection indexes can be obtained by the proposed CPL-BNNM algorithm. When dataset is collected, more data points are obtained by the retention algorithms. With the property of passing the "middle" data points, the principal curve has a certain ability to process the data error. Hence, the requirement of data acquisition accuracy is reduced, so the proposed CPL-BNNM algorithm is more favorable for practical application.

According to Fig. 13, considering that the dotted line 1 shows the crack which the CSI algorithm appears, it is easy to verify the superiority of the proposed CPL-BNNM algorithm to deal with the closed dataset. In this way, we only use

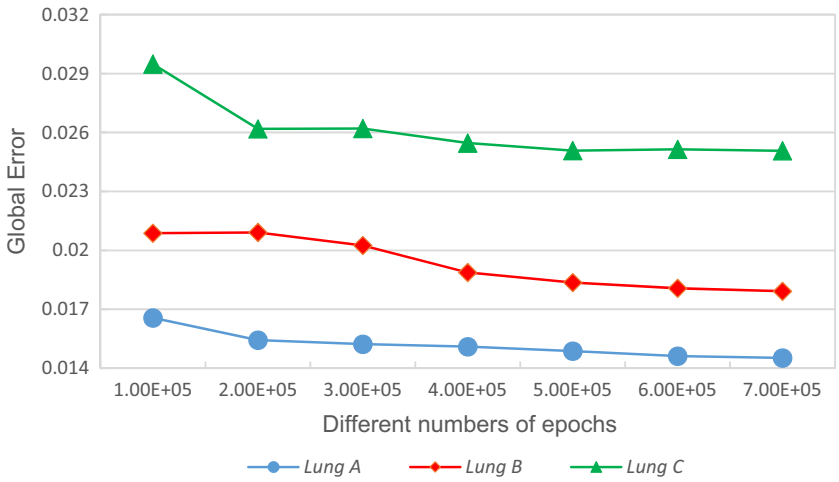

Fig. 11 Corresponding E at different numbers of epochs

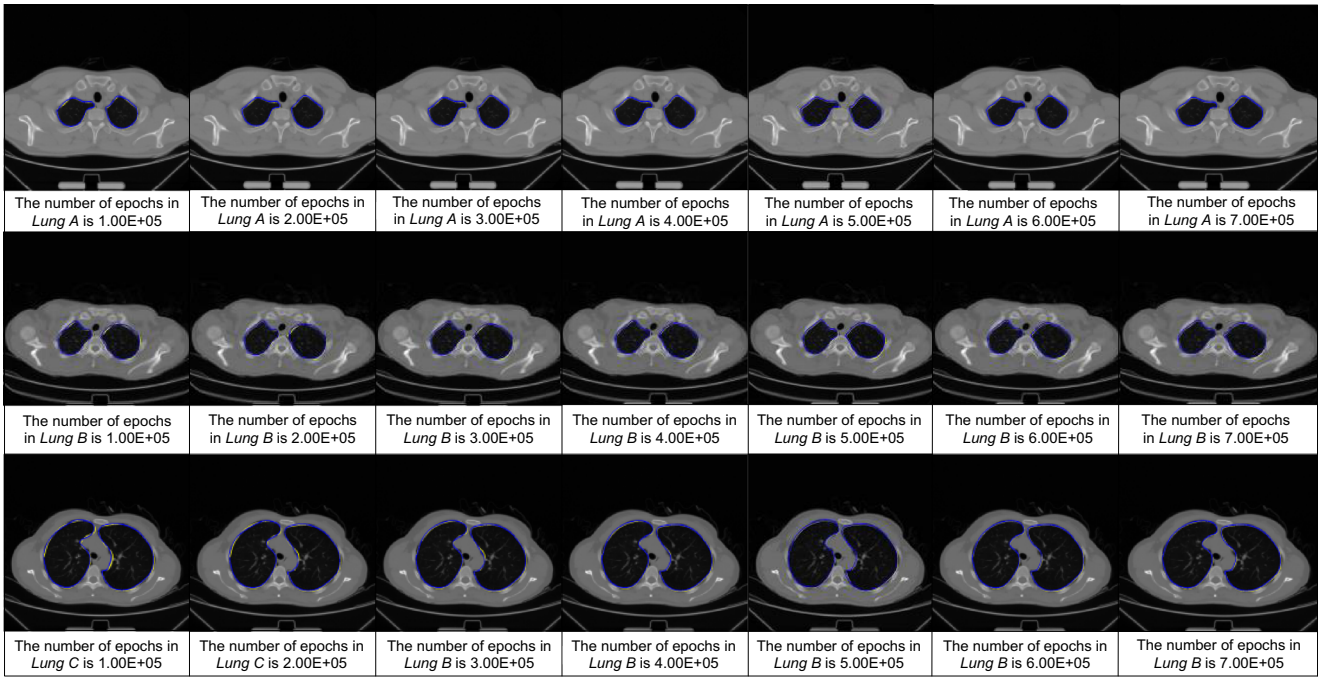

Fig. 12 Comparison between the contours obtained by the proposed algorithm and the manual contours at different numbers of epochs

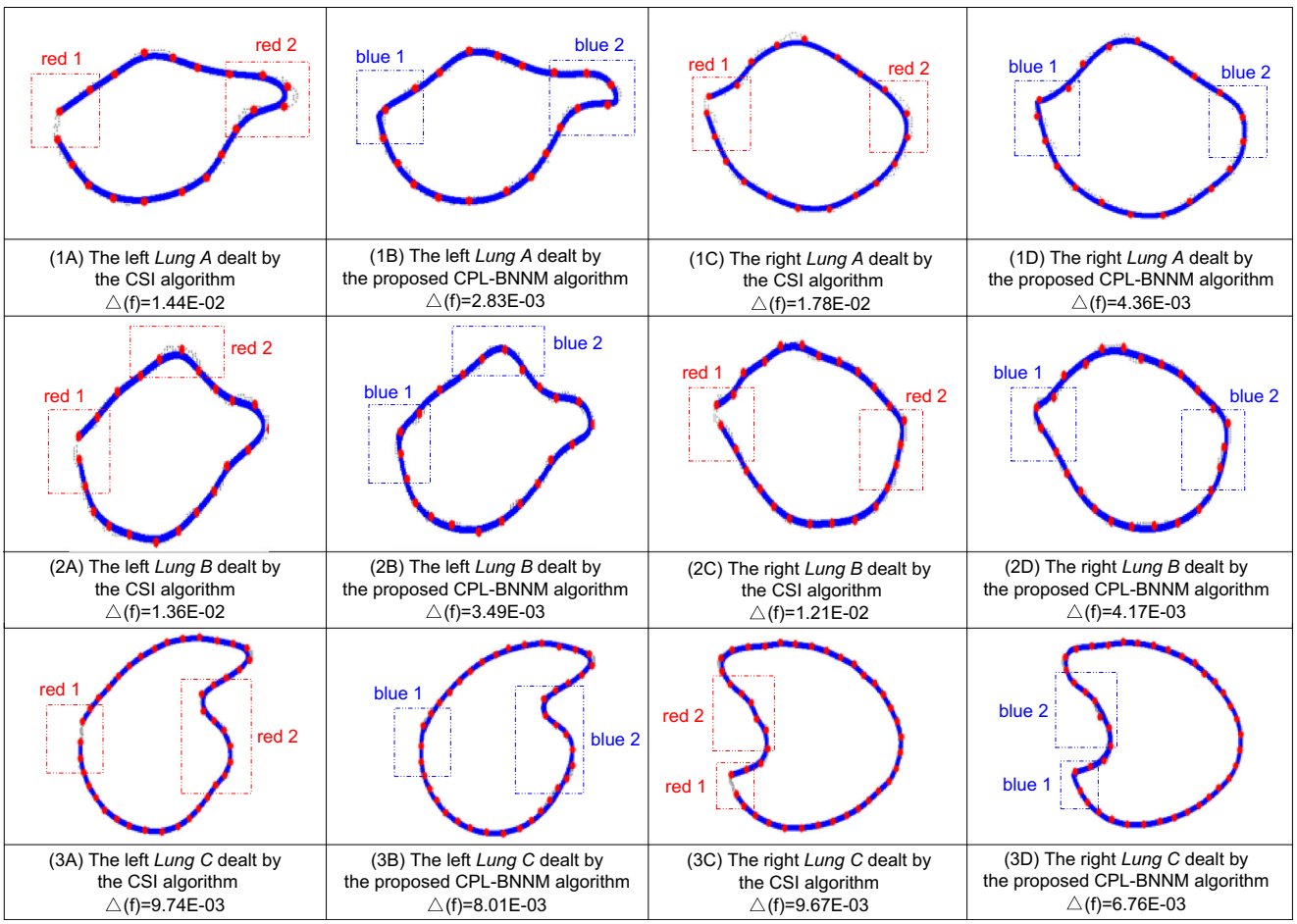

Fig. 13 Global comparison graph of curve fitting

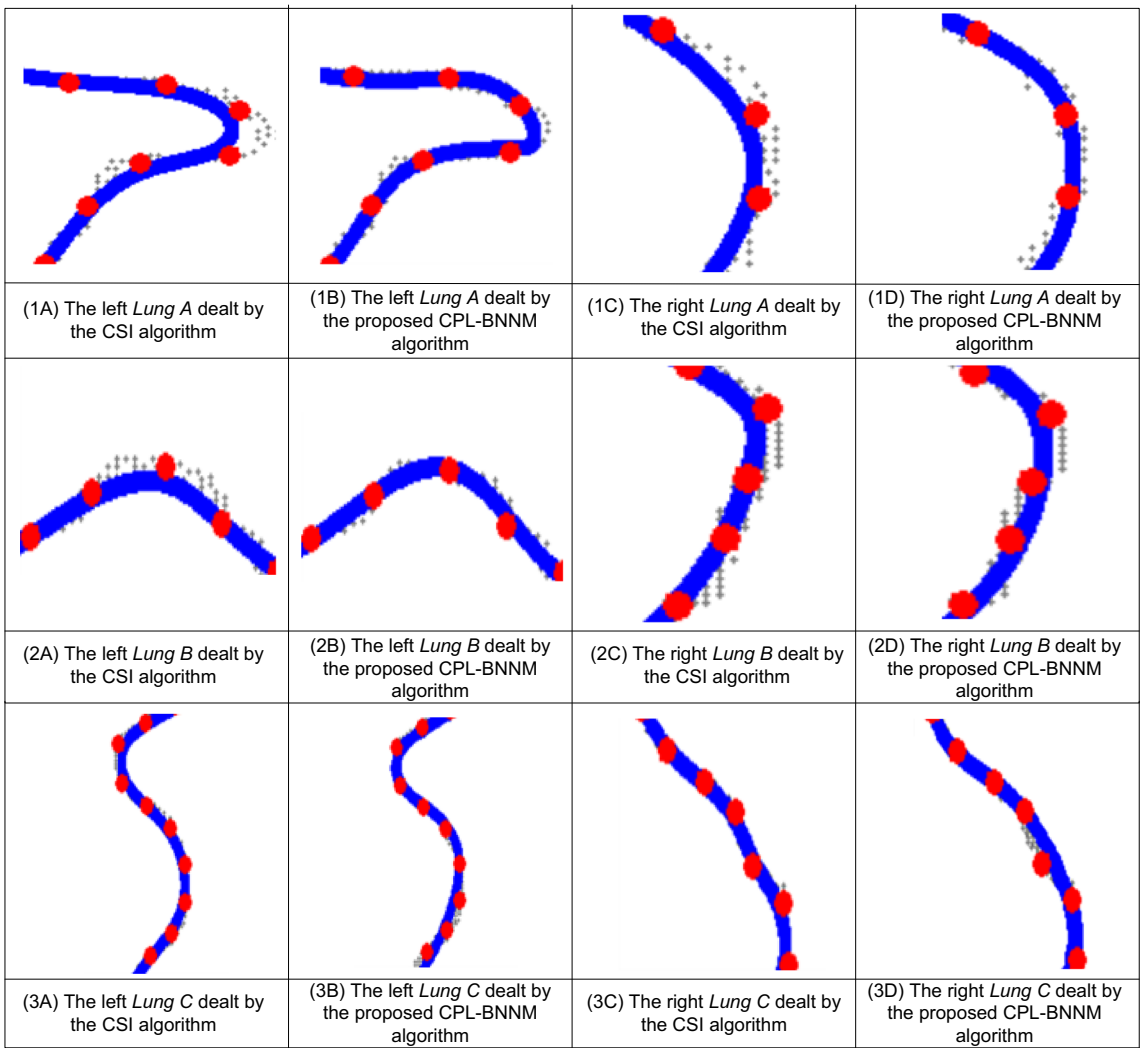

Fig. 14 Partial magnification graph of curve fitting

the dotted line 2 in Fig. 13 for analysis in which Fig. 14 can be gotten to show the partial magnification graph of curve fitting. Because of more characteristic of *Lung B* than others, *Lung B* is mainly analyzed. From Fig. 14, each pixel point of the dataset is too small to observe, in order to improve the contrast of the experimental results; the cross form will be used to denote each pixel of the dataset in this paper. It can be seen from Fig. 14(2A), (2B) that when the turn occurs, the principal curve obtained by the CSI algorithm is more deviated from the approximate trajectory of the initial points. The reason is that the robust ability of the obtained principal curve is weakened by the influence of the excessive oscillation. On the contrary, with continuous training in the proposed CPL-BNNM algorithm, the complete and smooth expression of the principal curve can be acquired. In addition, the center position which the principal curve processes the initial points is recorded as

Table 1 Comparison of proposed study with previous works (Dice values in mean ± standard deviation)

Authors, years	Technique/method	Database	Dice coefficient
Proposed method	CPL-BNNM	LIDC-IDRI	0.83 ± 0.11
Wang et al., 2017 [47]	Multi-view deep convolutional neural network	LIDC-IDRI	0.78 ± 0.16
Wang et al., 2017 [48]	Central Focused Convolutional Neural Networks	LIDC-IDRI	0.82 ± 0.11
Song et al., 2016 [49]	Toboggan Based Growing Automatic segmentation	LIDC-IDRI	0.81 ± 0.04
Kubota et al., 2011 [50]	Distance transform, region growing, convex hull	LIDC-IDRI	0.69 ± 0.18
Lavdas et al., 2017 [37]	3D Convolutional Neural Network	Private	0.81 ± 0.13

well. So that the fitting problem of the complex data distribution is solved, while the mathematical expression of lung image based on the principal curve can be obtained.

By looking at the results of Fig. 14(2C), (2D), it is observed that when the dataset is very much or the curvature of the obtained curve is very large, the obtained curves of the CSI and the proposed CPL-BNNM algorithm are all deviated from the center lines. Intuitively, the achieved curve of the CSI algorithm seems to be much closer to the approximate trajectory of the dataset, but the curve obtained by the proposed CPL-BNNM algorithm covers the more initial points relatively. In addition, the curve achieved by the proposed CPL-BNNM algorithm can be repaired automatically to approach the center of dataset by keeping on learning.

Contour Detection under Different Algorithms on Public LIDC-IDRI Dataset

To further validate the performance of the proposed algorithm, the public LIDC-IDRI dataset is used for experimental evaluation. All the ground truths in this dataset are verified and corrected by up to three board-certified radiologists. The public LIDC-IDRI database contains a different set of 1018 cases from seven institutions. All the CT scan images are stored in DICOM format with the size of pixels (512 × 512). The proposed method has been evaluated on 100 images from the public LIDC-IDRI dataset, which are randomly chosen. We compare our results to some current methods in lung segmentation. Table 1 describes the comparison of proposed study with previous works.

Conclusion

In CT images, detection and recognition of organs are problems in the field of image processing, and lung contour detection is one of the key problems in CT imaging. In this paper, we use the private dataset and the public LIDC-IDRI dataset to evaluate the proposed method, respectively. To the private dataset, the data points manually delineated by radiologists are treated as the initial dataset. The data sequences are generated by the CPL algorithm, where the data sequences are made up of the ordered projection indexes and the corresponding data points. The projection index is taken as the independent variable, while the initial data points are regarded as the dependent variable; the data sequence is trained by the BNNM, after that, the smooth contour of the lung can be obtained. With the proposed CPL-BNNM algorithm, the computational complexity of the contour extraction and the workload of radiologists can be reduced. The quantitative and qualitative experimental results show that our proposed semi-automatic detection method has better extraction accuracy for high-resolution lung datasets obtained by 3D-CT scans. A clear lung contour is retrieved by the proposed CPL-BNNM algorithm by training the data. While compared with other methods on the public LIDC-IDRI dataset, our method achieves superior segmentation performance with average Dice of 0.83. However, the BNNM can be too complex with excessive training and overfitting. In machine learning, overfitting is a common phenomenon; it will lead to the deviation between the actual output and the expected output to be very large. To solve the problem of overfitting, we plan to use the regularization or dropout to optimize the BNNM in the future. In addition, we plan to apply the proposed two-dimensional method into the three-dimensional medical reconstruction, which is based on the contour extraction of the two-dimensional lung image.

Acknowledgments The authors would like to thank the Second Affiliated Hospital of Soochow University for their support.

Funding Information This work was supported by the National Science Foundation of China (No. 61672369) and the National Natural Science Foundation of Jiangsu Province (Nos.17KJB520035 and 17KJB520037).

References

1. Ataer-Cansizoglu E, Bas E, Kalpathy-Cramer J, Sharp GC, Erdogmus D: Contour-based shape representation using principal curves. Pattern Recognition 46:1140–1150, 2013
2. Okumura E, Kawashita I, Ishida T: Computerized Classification of Pneumoconiosis on Digital Chest Radiography Artificial Neural Network with Three Stages. J Digit Imaging 30:1–14, 2017
3. Wang J, Kato F, Yamashita H, Baba M, Cui Y, Li R, Oyama-Manabe N, Shirato H: Automatic Estimation of Volumetric Breast Density Using Artificial Neural Network-Based Calibration of Full-Field Digital Mammography: Feasibility on Japanese Women With and Without Breast Cancer. J Digit Imaging 30:215–227, 2017
4. Kamra A, Jain VK, Singh S, Mittal S: Characterization of Architectural Distortion in Mammograms Based on Texture Analysis Using Support Vector Machine Classifier with Clinical Evaluation. J Digit Imaging 29:104–114, 2016
5. Song Y, Cai W, Zhou Y, Feng DD: Feature-based image patch approximation for lung tissue classification. IEEE Transactions on Medical Imaging 32:797–808, 2013
6. Brosch T, Tang LYW, Yoo Y, Li DKB, Traboulsee A, Tam R: Deep 3D convolutional encoder networks with shortcuts for multiscale feature integration applied to multiple sclerosis lesion segmentation. IEEE Transactions on Medical Imaging 35:1229–1239, 2016
7. Aarle WA, Batenburg KJ, Sijbers J: Optimal threshold selection for segmentation of dense homogeneous objects in tomographic reconstructions. IEEE Transactions on Medical Imaging 30:980–989, 2011
8. Zhao Y, Rada L, Chen K, Harding SP, Zheng Y: Automated vessel segmentation using infinite perimeter active contour model with hybrid region information with application to retinal images. IEEE Transactions on Medical Imaging 34:1797–1807, 2015
9. Barbu A, Suehling M, Xu X, Liu D, Zhou SK, Comaniciu D: Automatic detection and segmentation of lymph nodes from CT data. IEEE Transactions on Medical Imaging 31:240–250, 2012
10. Bates R, Irving B, Markelc B, Kaeppler J, Brown G, Muschel RJ, Brady M, Grau V, Schnabel JA: Segmentation of Vasculature from Fluorescently Labeled Endothelial Cells in Multi-Photon

Microscopy Images. IEEE Transactions on Medical Imaging 99:1–10, 2017
11. Ali S, Madabhushi A: An integrated region-, boundary-, shape-based active contour for multiple object overlap resolution in histological imagery. IEEE Transactions on Medical Imaging 31:1448–1460, 2012
12. Tang L, Niemeijer M, Reinhardt JM, Garvin MK, Abràmoff MD: Splat feature classification with application to retinal hemorrhage detection in fundus images. IEEE Transactions on Medical Imaging 32:364–375, 2013
13. Vogl WD, Waldstein SM, Gerendas BS, Schmidt-Erfurth U, Langs G: Predicting Macular Edema Recurrence from Spatio-Temporal Signatures in Optical Coherence Tomography Images. IEEE Transactions on Medical Imaging 36:1773–1783, 2017
14. Maggio S, Palladini A, Marchi LD, Alessandrini M, Speciale N, Masetti G: Predictive deconvolution and hybrid feature selection for computer-aided detection of prostate cancer. IEEE Transactions on Medical Imaging 29:455–464, 2010
15. Pu J, Fuhrman C, Good WF, Sciurba FC, Gur D: A differential geometric approach to automated segmentation of human airway tree. IEEE Transactions on Medical Imaging 30:266–278, 2011
16. Dai S, Lu K, Dong J, Zhang Y, Chen Y: A novel approach of lung segmentation on chest CT images using graph cuts. Neurocomputing 168:799–807, 2015
17. Zhou H, Goldgof DB, Hawkins S, Wei L, Liu Y, Creighton D, Gillies RJ, Hall LO, Nahavandi S: A robust approach for automated lung segmentation in thoracic CT. Proceedings of the 2015 I.E. conference on Systems, Man, and Cybernetics (SMC), Kowloon, China, 2015, pp 2267–2272
18. Tu L, Styner M, Vicory J, Elhabian S, Wang R, Hong J, Paniagua B, Prieto JC, Yang D, Whitaker R, Pizer SM: Skeletal Shape Correspondence through Entropy. IEEE Transactions on Medical Imaging 99:1–10, 2017
19. Shao Y, Gao Y, Guo Y, Shi Y, Yang X, Shen D: Hierarchical lung field segmentation with joint shape and appearance sparse learning. IEEE Transactions on Medical Imaging 33:1761–1780, 2014
20. Soliman A, Khalifa F, Elnakib A, El-Ghar MA, Dunlap N, Wang B, Gimel'farb G, Keynton R, El-Baz A: Accurate lungs segmentation on CT chest images by adaptive appearance-guided shape modeling. IEEE Transactions on Medical Imaging 36:263–276, 2017
21. Dhara AK, Mukhopadhyay S, Dutta A, Garg M, Khandelwal N: A combination of shape and texture features for classification of pulmonary nodules in lung ct images. J Digit Imaging 29:466–475, 2016
22. Nguyen HV, Porikli F: Support vector shape: A classifier-based shape representation. IEEE Transactions on Pattern Analysis and Machine Intelligence 35:970–982, 2013
23. Deng C, Lin H: Progressive and iterative approximation for least squares B-spline curve and surface fitting. Computer-Aided Design 47:32–44, 2014
24. Xiao C, Staring M, Shamonin D, Reiber JHC, Stolk J, Stoel BC: A strain energy filter for 3D vessel enhancement with application to pulmonary CT images. Medical Image Analysis 15:112–124, 2011
25. Shepherd T, Prince SJD, Alexander DC: Interactive lesion segmentation with shape priors from offline and online learning. IEEE Transactions on Medical Imaging 31:1698–1712, 2012
26. Song Q, Bai J, Garvin MK, Sonka M, Buatti JM, Wu X: Optimal multiple surface segmentation with shape and context priors. IEEE Transactions on Medical Imaging 32:376–386, 2013
27. Zhang S, Zhan Y, Metaxas DN: Deformable segmentation via sparse representation and dictionary learning. Medical Image Analysis 16:1385–1396, 2012
28. Heibel H, Glocker B, Groher M, Pfister M, Navab N: Interventional tool tracking using discrete optimization. IEEE Transactions on Medical Imaging 32:544–555, 2013
29. Aquino A, Gegúndez-Arias ME, Marín D: Detecting the optic disc boundary in digital fundus images using morphological, edge detection, and feature extraction techniques. IEEE Transactions on Medical Imaging 29:1860–1869, 2010
30. Li Z, Zhang Y, Liu G, Shao H, Li W, Tang X: A robust coronary artery identification and centerline extraction method in angiographies. Biomedical Signal Processing and Control 16:1–8, 2015
31. Hastie T, Stuetzle W: Principal curves. Journal of the American Statistical Association 84:502–516, 1989
32. Bradley RS, Withers PJ: Post-processing techniques for making reliable measurements from curve-skeletons. Computers in biology and medicine 72:120–131, 2016
33. Kégl B, Krzyzak A: Piecewise linear skeletonization using principal curves. IEEE Transactions on Pattern Analysis and Machine Intelligence 24:59–74, 2002
34. Yu Y, Wang J: Enclosure Transform for Interest Point Detection From Speckle Imagery. IEEE Transactions on Medical Imaging 36:769–780, 2017
35. Khedher L, Ramírez J, Górriz JM, Brahim A, Segovia F: Early diagnosis of Alzheimer' s disease based on partial least squares, principal component analysis and support vector machine using segmented MRI images. Neurocomputing 151:139–150, 2015
36. Zhu X, Ge Y, Li T, Thongphiew D, Yin FF, Wu QJ: A planning quality evaluation tool for prostate adaptive IMRT based on machine learning. Medical physics 38:719–726, 2011
37. Lavdas I, Glocker B, Kamnitsas K, Rueckert D, Mair H, Sandhu A, Taylor SA, Aboagye EO, Rockall A: G: Fully automatic, multiorgan segmentation in normal whole body magnetic resonance imaging (MRI), using classification forests (CFs), convolutional neural networks (CNNs), and a multi-atlas (MA) approach. Medical Physics 44:5210–5220, 2017
38. Tseng HH, Luo Y, Cui S, Chien JT, Ten Haken RK, Naqa IE: Deep reinforcement learning for automated radiation adaptation in lung cancer. Medical Physics 44:6690–6705, 2017
39. Ma J, Wu F, Jiang TA, Zhu J, Kong D: Cascade convolutional neural networks for automatic detection of thyroid nodules in ultrasound images. Medical Physics 44:1678–1691, 2017
40. Shaukat F, Raja G, Gooya A, Frangi AF: Fully automatic detection of lung nodules in CT images using a hybrid feature set. Medical Physics 44:3615–3629, 2017
41. Taigman Y, Yang M, Ranzato MA, Wolf L: Deepface: Closing the gap to human-level performance in face verification. Proceedings of the 27th IEEE conference on computer vision and pattern recognition, Columbus, USA, 2014, pp 1701–1708
42. Najafabadi MM, Villanustre F, Khoshgoftaar TM, Seliya N, Wald R, Muharemagic E: Deep learning applications and challenges in big data analytics. Journal of Big Data 2:1, 2015
43. Kégl B, Krzyzak A, Linder T, Zeger K: Learning and design of principal curves. IEEE Transactions on Pattern Analysis and Machine Intelligence 22:281–297, 2000
44. Armato SG, McLennan G, Bidaut L et al.: The lung image database consortium (LIDC) and image database resource initiative (IDRI): a completed reference database of lung nodules on CT scans. Medical Physics 38:915–931, 2011
45. Srivastava N, Hinton GE, Krizhevsky A, Sutskever I, Salakhutdinov R: Dropout: a simple way to prevent neural networks from overfitting. Journal of machine learning research 15: 1929–1958, 2014
46. LeCun Y, Bengio Y, Hinton GE: Deep learning. Nature 521:436–444, 2015
47. Wang S, Zhou M, Gevaert O, Tang Z, Dong D, Liu Z, Tian J: A multi-view deep convolutional neural networks for lung nodule segmentation. Proceedings of the 39th Annual International Conference of the IEEE Engineering in Medicine and Biology Society (EMBC), Jeju Island, South Korea, 2017, pp 1752–1755

48. Wang S, Zhou M, Liu Z, Liu Z, Gu D, Zang Y, Dong D, Gevaert O, Tian J: Central focused convolutional neural networks: Developing a data-driven model for lung nodule segmentation. Medical image analysis 40:172–183, 2017
49. Song J, Yang C, Fan L, Wang K, Yang F, Liu S, Tian J: Lung lesion extraction using a toboggan based growing automatic segmentation approach. IEEE transactions on medical imaging 35:337–353, 2016
50. Kubota T, Jerebko AK, Dewan M, Salganicoff M, Krishnan A: Segmentation of pulmonary nodules of various densities with morphological approaches and convexity models. Medical Image Analysis 15:133–154, 2011